BATTERIES

Dynamics of particle network in composite battery cathodes

Jizhou Li[1]†, Nikhil Sharma[2]†, Zhisen Jiang[1], Yang Yang[3]‡, Federico Monaco[3], Zhengrui Xu[4], Dong Hou[4], Daniel Ratner[5], Piero Pianetta[1], Peter Cloetens[3], Feng Lin[4]*, Kejie Zhao[2]*, Yijin Liu[1]*

Improving composite battery electrodes requires a delicate control of active materials and electrode formulation. The electrochemically active particles fulfill their role as energy exchange reservoirs through interacting with the surrounding conductive network. We formulate a network evolution model to interpret the regulation and equilibration between electrochemical activity and mechanical damage of these particles. Through statistical analysis of thousands of particles using x-ray phase contrast holotomography in a $LiNi_{0.8}Mn_{0.1}Co_{0.1}O_2$-based cathode, we found that the local network heterogeneity results in asynchronous activities in the early cycles, and subsequently the particle assemblies move toward a synchronous behavior. Our study pinpoints the chemomechanical behavior of individual particles and enables better designs of the conductive network to optimize the utility of all the particles during operation.

Lithium-ion batteries (LIBs), with a high energy density and long lifetime, have been widely adopted for a broad range of applications. The composite cathode of LIBs is made of many electrochemically active particles embedded in a conductive carbon and binder matrix. The microstructure plays a crucial role in governing the LIB performance through modulating the electronic and ionic transport properties (*1*, *2*) and the chemomechanical behavior (*3*–*5*). The cracking, disintegration, and (de)activation behaviors of the electrochemically active cathode particles affect the capacity fade over prolonged battery cycling (*6*–*8*).

Alleviation of the active particle damage has focused on understanding and tuning the morphological and chemical characteristics at the microscale (*9*–*12*), such as particle size, elongation and sphericity (*13*, *14*), crystallographic arrangement (*15*, *16*), mesoscale kinetics (*17*, *18*), grain boundary properties (*19*, *20*), and compositional variation (*21*–*24*). For instance, reducing the primary particle size is an effective approach to improving the fast-charging performance because smaller particles have shorter ion diffusion paths (*25*, *26*). Designing particles with elongated morphology, e.g., in the form of nanoplates or nanorods, can also improve the specific capacity and reduce charge transfer resistance (*27*). However, the correlation between the particle morphology and the cell performance is rather complex, with effects at multiple length and time scales. The dynamics of particle network have substantial impacts but are rarely studied. For example, recent studies have uncovered the local heterogeneity in the electrode, where active particles contribute to the cell-level chemistry differently in time and position (*28*). Some particles release lithium ions at a faster rate than their peers under fast-charging conditions (*29*). Some local regions could become inactive while the cell can still function well as a whole. To make a substantial improvement effectively, the particle structure and the electrode morphology should be tailored coherently, and a synergy could be achieved by doing so. A global homogenization will eventually develop after long-term cycling; however, a poorly designed electrode would reach this state when most of its particles are severely damaged. By contrast, a well-formed electrode would rapidly converge to the electrode synchronization with most of its particles still intact. In our study, we image thick Ni-rich composite cathode electrodes with a multilayer of $LiNi_{0.8}Mn_{0.1}Co_{0.1}O_2$ (NMC) particles at different states using nano-resolution hard x-ray phase contrast holotomography (Fig. 1A). These electrodes are recovered from standard coin cells that were cycled under fast-charging conditions for 10 cycles and 50 cycles (fig. S1), respectively. With high spatial resolution and contrast, and a large field of view, our three-dimensional imaging data cover a large number of active particles that demonstrate a wide variety of damage patterns. To facilitate a statistical analysis, we build on our previous neural network–based particle identification method (*1*) and improve its accuracy and efficiency by developing a diagonal data fusion approach, which is illustrated in figs. S2 and S3. Upon completion of the particle identification using this method, the damage level of individual particles is further quantified. The relative probability distribution of the particle damage degree is presented in Fig. 1B, and a few randomly

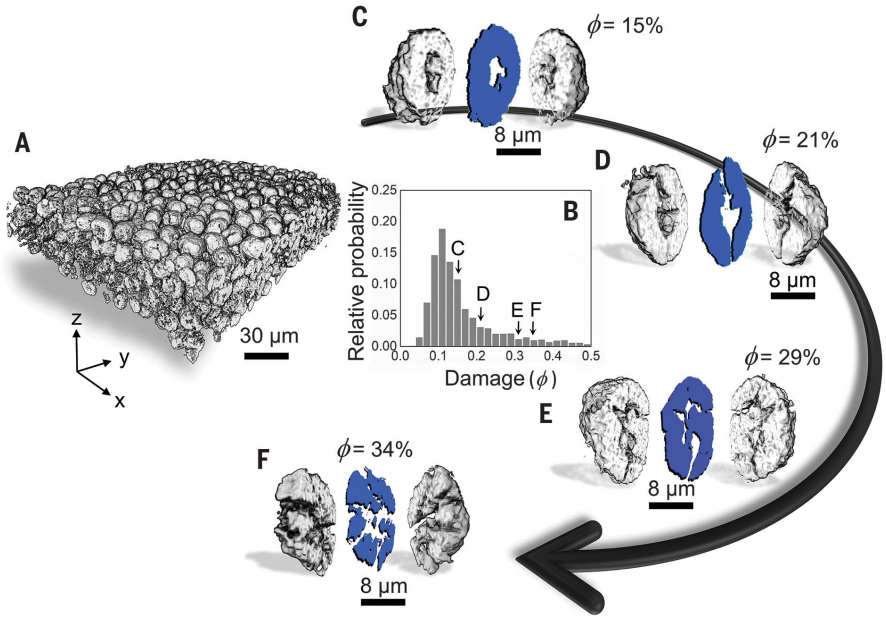

Fig. 1. Imaging cathode electrodes with a multilayer of NMC particles using nano-holotomography. (**A**) Visualization of the composite battery cathode obtained by synchrotron nano-holotomography. Each NMC particle has its own properties in position, particle structure, mesoscale chemistry, and local morphology. (**B**) Probability distribution of the particle damage level. (**C** to **F**) Randomly selected examples of NMC particles with different levels of damage.

[1]Stanford Synchrotron Radiation Lightsource, SLAC National Accelerator Laboratory, Menlo Park, CA 94025, USA. [2]School of Mechanical Engineering, Purdue University, West Lafayette, IN 47906, USA. [3]European Synchrotron Radiation Facility, Grenoble 38000, France. [4]Department of Chemistry, Virginia Tech, Blacksburg, VA 24061, USA. [5]Machine Learning Initiative, SLAC National Accelerator Laboratory, Menlo Park, CA 94025, USA.
***Corresponding author. Email: fenglin@vt.edu (F.L.); kjzhao@purdue.edu (K.Z.); liuyijin@slac.stanford.edu (Y.L.)**
†These authors contributed equally to this work.
‡Present address: National Synchrotron Light Source II, Brookhaven National Laboratory, Upton, NY 11973, USA.

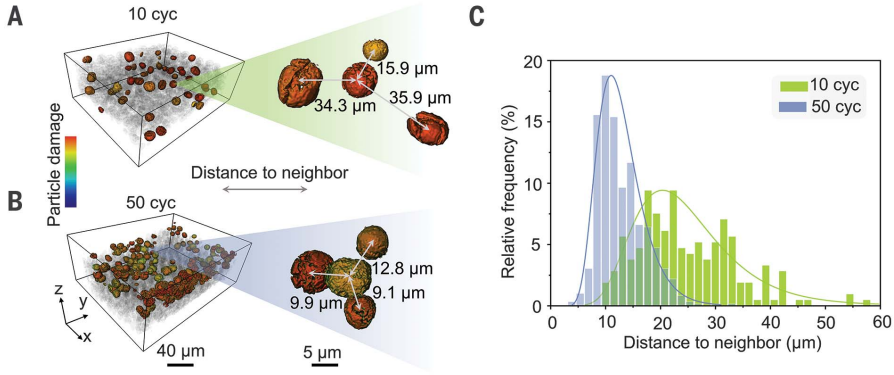

Fig. 2. Heterogeneous particle damage in battery electrodes. The spatial distributions of the severely damaged particles in the (A) 10-cycled and (B) 50-cycled electrodes. The degree of particle damage is color coded. Selected representative regions are enlarged for better visualization. The distances between the central damaged particle and its three nearest-neighboring damaged particles are annotated in the enlarged view. (**C**) Probability distributions of the distance between two neighboring severely damaged particles in 10-cycled and 50-cycled electrodes.

selected particles with different damage patterns are highlighted in Fig. 1, C to F.

The severely damaged particles are those overused during the electrochemical fast-charging process. Their spatial distribution and arrangement are evidence of the spatially heterogeneous electrode utility. As shown in Fig. 2, A and B, the severely damaged particles are sparsely distributed in the 10-cycled electrode and, their concentration increased upon further cycling, featuring a denser agglomeration in the 50-cycled electrode (as illustrated in the enlarged views). Figure 2C shows the probability distributions of the distance between two neighboring severely damaged particles in 10-cycled and 50-cycled electrodes, respectively. A shift toward shorter distance can be observed in the 50-cycled electrode, indicating a synchronization effect within the local particle clusters.

We perform theoretical modeling to understand the damage and Li reaction behaviors of NMC particles across cycles. We envision that the interplay between the electrochemical activity and the mechanical damage regulates the performance of the NMC particles. The deeper state of charge incurs more severe consequences, such as the particle damage and decohesion of particles from the conductive agent. By contrast, the mechanical damage increases the cost of Li reactions and suppresses the electrochemical activity of individual particles. A more synchronous behavior of the composite cathode is achieved in the prolonged cycles because of the equilibrium between the electrochemical activity and mechanical damage. To test this hypothesis, we conducted finite element analysis to model the electrochemical response and mechanical damage of a NMC cathode composed of three spherical NMC active particles surrounded by two homogeneous porous carbon/binder (CB) domains of different electrical conductivities (Fig. 3). The intention of the computational model is not to capture all the explicit microstructural details in the composite cathode. Rather, our goal is to replicate the salient feature in the composite such that the active NMC particles are covered by different degrees of the electrically conductive agent, which results in various local conducting networks for individual particles. In this simplified model, the surrounding high-conductivity and low-conductivity CBs differ in their electrical conductivities. The model assumes that liquid electrolyte is soaked in the porous CB domains and thus the NMC particles are fully accessible to the Li^+ in the liquid electrolyte. We set different ratios of coverage of CB on the periphery of each active particle, as illustrated in Fig. 3A. The interface of active particles attached to the high-conductivity CB undergoes a faster electrochemical reaction than the boundary enclosed by the low-conductivity CB. Thus, each active particle experiences dissimilar electrochemical activities, as inferred from the diverging concentration profiles (C/C_{max}) during the first charging process (Fig. 3B).

The modulation between the electrochemical activity and mechanical damage reduces the variation of Li concentration with the progression of (dis)charge cycles. As shown in the normalized Li concentration plot (Fig. 3B) and the plot of the Li concentration variation across the three NMC particles (Fig. 3C), the concentration profiles converge with battery operation. During the charging process, Li extraction generates a reduction of the lattice volume in the NMC particles (*30*). Considerable variation in the mechanical properties of the NMC particles (elastic modulus ~ 140 GPa) and CB (elastic modulus ~ 2 GPa) generates strain mismatch at the interface. The apex of the mismatch occurs near the end of the charging process, as demonstrated by the divergence of the damage profiles in Fig. 3D and their corresponding differences to the mean damage in Fig. 3E.

After the onset of heterogeneous damage among the NMC particles, the individual damage curves diverge (Fig. 3D). The individual NMC particle characteristic—i.e., the dissimilar coverage by high- and low-conductivity CBs—commands the degree of heterogeneous damage in the early cycles. With successive discharging and charging processes, the modulation between electrochemical activity and mechanical damage reduces the imbalance within the system (through the interfacial resistance for charge transfer). Consequently, the damage level for all three particles converges, demonstrating the system's progression toward a synchronized behavior. In addition, we observe a similar transformation to synchronized damage behavior for the system with more NMC active particles (fig. S4). The variation in the periphery contact with high- and low-conductivity CB regions generates heterogeneous reactions for each particle. After the initial divergence, the individual particle damage is tuned by the feedback to electrochemical activity that progresses toward a synchronized behavior in the composite electrode.

Both the particle damage and Li concentration profiles theoretically confirm the asynchronous to synchronous evolution in composite cathodes. Such a transition can occur for a number of reasons, such as from the particles' self-attributes, interactions with neighboring particles, and CB domains. To probe the evolution mechanisms from the intrinsic or internal physical nature of cathode particles, we analyzed the three-dimensional tomographic imaging data through an interpretable machine learning framework.

Using more than 2000 accurately identified NMC particles, we extract their structural, chemical, and morphological characteristics. More specifically, we divided the particle attributes into four different groups: position, chemical properties, particle structure, and local morphology (as illustrated in table S1 and fig. S5; in total, 24 attributes are extracted). As indicated in fig. S6, these extracted particle attributes demonstrate varying characteristics in their respective probability distributions. Revealing their interrelationship is not straightforward and could benefit from more advanced computing and modeling approaches.

We leverage the advances in machine learning to model relationship and dependencies among attributes, i.e., descriptors of the cathode particles' properties (fig. S7). The model has to be both accurate and interpretable. To elucidate the intertwined limiting factors for battery cathode robustness, we explore the degree of

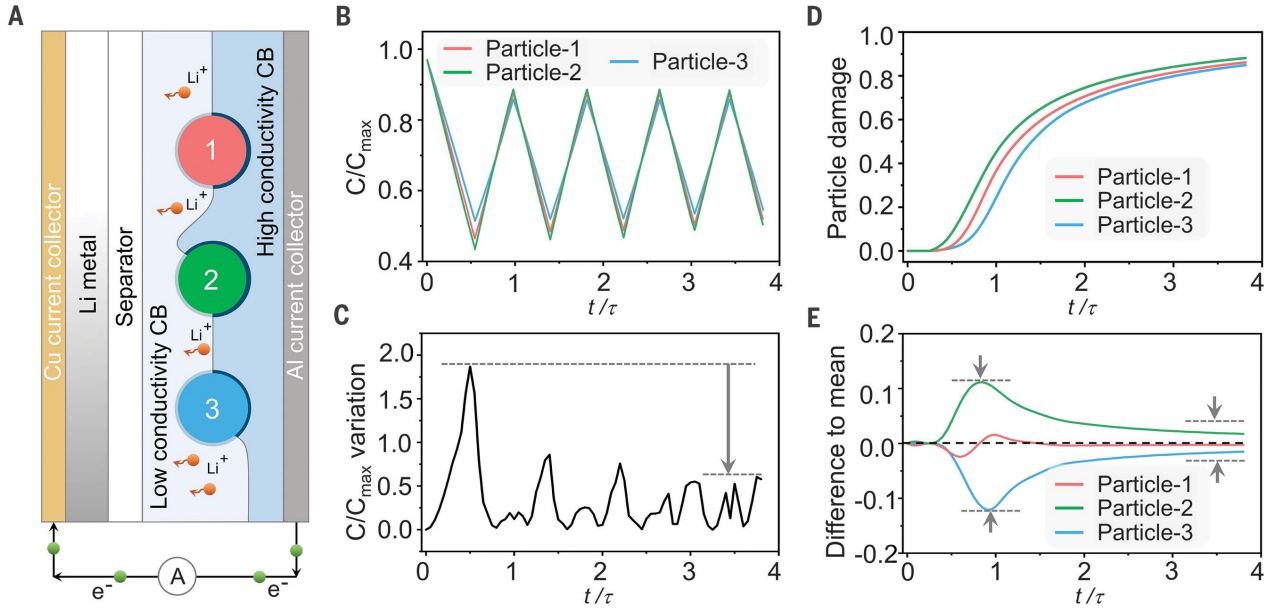

Fig. 3. Finite element analysis of the electrochemical activity and mechanical damage in the NMC cathode. (**A**) Illustration of the composite model during the charging process in the battery. (**B**) Normalized Li concentration profiles depict the inherent heterogeneity of the system during the first charging process with respect to the normalized time t/τ, where t is the real time in Li reactions and τ = 720 s is the theoretical time to reach the full capacity of NMC. Although the particles start with the same state of charge, Li concentration differs at the end of the first charge process. (**C**) The variation of Li concentration profiles among three NMC particles. The overall trend demonstrates the tendency toward a synchronized behavior. (**D**) The damage profiles for three NMC active particles diverge near the end of the first charge process. With the progression of the cycling process, the damage profiles for all three particles converge. (**E**) Each particle's deviation from the mean damage profile (the black dashed line).

cathode NMC particles' engagement in the cell-level chemistry through attribute correlation and damage regression. These two steps are accomplished using a regularized autoencoder neural network (*31*) and random forest (RF) regression (*32*). The SHAP (Shapley additive explanations) (*33*) is utilized to rank the importance of the particle properties to the degree of particle damage during the process of regression, which effectively reveals the contributions of different microstructural characteristics to the damage profile for every particle in our electrode. The circular plot (*34*) is used for better visualization of the Pearson's correction among different particle attributes. Integrated with the SHAP values, the RF provides not only accurate regression results, but also the interpretability of the impacts of all the input attributes on individual predictions as well as global insights.

Specifically, the autoencoder neural network compresses the input attributes into latent dimension (LDs) through an encoder network (fig. S8), which has been extensively applied for scientific discovery because of its ability to learn nonlinear functions and its good interpretability (*35*, *36*). The LDs of both datasets for 10-cycled and 50-cycled electrodes, respectively, are calculated and are subsequently correlated with each other through Pearson's correlation. As shown in fig. S9, different LDs show intertwined relationships in both cases. Each node in the circular plot represents one LD, and a connection between two nodes indicates a relatively high correlation between them. The sign of the correlation coefficient (+/−) defines the direction of the relationship. For the 10-cycled electrode, the first five LDs appear to be independent. As more LDs are added, we start to observe correlations among them. For the 50-cycled electrode, in addition to the common connections, several additional correlations emerge (as highlighted by the dark colors in fig. S9D). The observation of a higher degree of interdependence among different LDs indicates that the particles' structural and chemical characteristics become more intertwined upon battery cycling.

When interpreting the model regression results with the SHAP values, which utilize the game-theory–based Shapley values (*37*), the contribution of each attribute to the model's output (the particle damage degree) can be obtained. Attributes with larger SHAP values are considered to be more important to the target damage degree. The contribution scores of all attributes to the particle damage in both 10-cycled and 50-cycled electrodes are presented in Fig. 4 (attributes are grouped on the basis of their properties and reordered for better visualization), and the interpretation is provided below. The advantage of using SHAP to explain the regression model is its superior robustness to correlated attributes compared to the traditional methods (*38*), e.g., the Pearson's correlation, which cannot systematically capture the key differences in the studied electrodes (fig. S11).

From our model-based prediction in Fig. 4, some of the attributes follow expected trends. For example, the particle's depth, *Z*, affects the particle damage (*28*, *39*). This can be related to the cell polarization effect, which results in particles at different depths experiencing different states of charge at a given time. The *Z*-dependence of particle damage is more pronounced in the 10-cycled electrode, in good agreement with previous reports (*9*, *28*). The electron density, *EDensity*, has been associated with the state of charge (*1*) and its averaged value and degree of variation, *Homogeneity*, shows considerable impact on the particle damage throughout the cycling process. The surface area and roughness (*RoughOuter*, *RoughInner*, *SurfOuter*, and *SurfInner*; table S1) could affect the cohesion of the active particles and the CB matrix. Therefore, the surface characteristics could affect the particle damage. The particle's size, *Volume*, appears to be correlated with the particle damage. Its contribution score seems slightly lower in the 50-cycled electrode. This trend suggests that the particle-size effect might

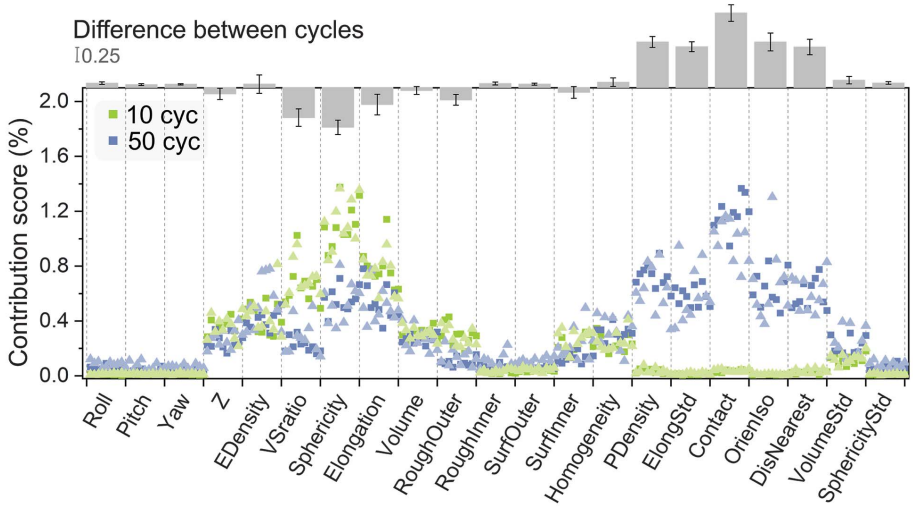

Fig. 4. Interpretable machine learning framework for particle attributes modeling. The contribution scores of all attributes to the particle damage in 10-cycled (green) and 50-cycled (blue) electrodes. Triangle and square markers represent results from two robustness validation approaches, data-subsampling and random-seeding, respectively. The mean and SD of the differences in the contribution scores (N = 20) between the 10-cycled and 50-cycled data are plotted on the top.

not be the limiting factor in the later cycles. However, the variation of the neighboring particles' volumes, *VolumeStd*, shows an opposite trend, featuring a higher contribution score in the 50-cycled electrode. This observation indicates that, upon prolonged battery operation, the uniformity in the neighboring particle size becomes a more relevant factor that affects the particle damage. Mixing particles of different sizes has been used as a method to improve the electrode's packing density. Our result suggests that this approach should be carefully examined from the long-term cyclability perspective. Another finding is that the particle elongation, *Elongation*, which represents the ratio of the longest axis length to the shortest axis length (table S1), has a rather high contribution score, which, however, decreases upon cycling. By contrast, the alignment of the neighboring particles, *OrienIso*, which shows negligible contribution in the 10-cycled electrode, becomes more important in the later cycles. In advanced battery electrode manufacturing, particle alignment can be purposely adjusted by controlling externally applied electric and/or magnetic fields (*40*–*42*).

When visualizing the overall picture of our statistical analysis over thousands of particles, we find an interesting pattern: In the early cycles, individual particles' characteristics (e.g., the position *Z*, *VSratio*, *Sphericity,* and *Elongation*; table S1) predominantly determine their respective degrees of damage, featuring an asynchronous behavior that is in agreement with our theoretical modeling result. In the later cycles, however, the interplay among neighboring particles (e.g., *Contact*, *DisNearest*, *OrienIso*, and *PDensity*) becomes more important, which indicates that the local interparticle arrangement can critically affect the asynchronous-to-synchronous transition. The mean difference and standard deviation (SD) of each attribute's contribution scores between the 10-cycled and 50-cycled datasets is presented on the top of Fig. 4, featuring a valley on the left and a peak on the right, supporting the above-described observation.

Our experimental observations (Fig. 2) and machine learning analysis (Fig. 4) collectively corroborate the theoretical modeling (Fig. 3). These results reveal a transition from the asynchronous behavior in the early stage toward a synchronous state later in the particle network evolution, where the interplay among neighbor particles plays a facilitating role (fig. S12). Particles' self-attributes, together with the dynamic nature of the conductive network, jointly determine the damage behavior of NMC particles in composite electrodes. These are critical factors for cathode design to prolong the cycle life of batteries. On the basis of our results, in the active cathode powder, it is useful to suppress the particle-to-particle variation in their structural characteristics, such as particle size, sphericity, elongation, etc. At the electrode scale, an ordered particle arrangement is favorable, which can be reinforced through a field-guided approach. Whereas the in-plane homogeneity is desirable, in the out-of-plane direction, a structural gradient could be beneficial because of the electrochemical polarization, which is more severe in thick electrodes. To summarize, an ordered electrode configuration with tailored depth-dependent packing of uniform active particles would be robust to prolonged battery cycling.

From the synthesis perspective, the particle shape and structure can be tuned by controlling the sintering temperature, incorporation of trace-element doping, designing the architecture of the precursor, and surface coating. These are common synthesis strategies and can be scalable for mass production. For the electrode manufacturing, the field-guided approach has been demonstrated to be effective for creating an ordered structure. This is compatible with the existing electrode manufacturing facilities and, thus, can be fairly cost effective.

REFERENCES AND NOTES

1. Z. Jiang *et al*., *Nat. Commun.* **11**, 2310 (2020).
2. D. E. Stephenson *et al*., *J. Electrochem. Soc.* **158**, A781 (2011).
3. R. Xu *et al*., *J. Mech. Phys. Solids* **129**, 160–183 (2019).
4. Z. Xu *et al*., *J. Mater. Chem. A* **6**, 21859–21884 (2018).
5. L. Mu *et al*., *Nano Lett.* **18**, 3241–3249 (2018).
6. Z. Yang, F. Lin, *J. Phys. Chem. C* **125**, 9618–9629 (2021).
7. H. Liu *et al*., *Nano Lett.* **17**, 3452–3457 (2017).
8. Y. Mao *et al*., *Adv. Funct. Mater.* **29**, 1900247 (2019).
9. F. Lin, K. Zhao, Y. Liu, *ACS Energy Lett.* **6**, 4065–4070 (2021).
10. H. H. Sun *et al*., *ACS Energy Lett.* **5**, 1136–1146 (2020).
11. W. E. Gent *et al*., *Adv. Mater.* **28**, 6631–6638 (2016).
12. X. Lu *et al*., *Nat. Commun.* **11**, 2079 (2020).
13. X. Liu *et al*., *Adv. Energy Mater.* **11**, 2003583 (2021).
14. W. Li, E. M. Erickson, A. Manthiram, *Nat. Energy* **5**, 26–34 (2020).
15. Z. Xu *et al*., *Nat. Commun.* **11**, 83 (2020).
16. A. Liu *et al*., *J. Electrochem. Soc.* **168**, 050506 (2021).
17. A. J. Merryweather, C. Schnedermann, Q. Jacquet, C. P. Grey, A. Rao, *Nature* **594**, 522–528 (2021).
18. S. Kuppan, Y. Xu, Y. Liu, G. Chen, *Nat. Commun.* **8**, 14309 (2017).
19. M. Yoon *et al*., *Nat. Energy* **6**, 362–371 (2021).
20. J.-N. Zhang *et al*., *Nat. Energy* **4**, 594–603 (2019).
21. Y.-K. Sun *et al*., *Nat. Mater.* **8**, 320–324 (2009).
22. F. Lin *et al*., *Nat. Energy* **1**, 15004 (2016).
23. Z. Zhu *et al*., *Nat. Energy* **4**, 1049–1058 (2019).
24. H. H. Sun *et al*., *Nat. Commun.* **12**, 6552 (2021).
25. C. Delacourt, P. Poizot, S. Levasseur, C. Masquelier, *Electrochem. Solid-State Lett.* **9**, A352 (2006).
26. L. Bläubaum *et al*., *ChemElectroChem* **7**, 4755–4766 (2020).
27. D.-H. Kim, J. Kim, *J. Phys. Chem. Solids* **68**, 734–737 (2007).
28. Y. Yang *et al*., *Adv. Energy Mater.* **9**, 1900674 (2019).
29. J. Park *et al*., *Nat. Mater.* **20**, 991–999 (2021).
30. J. Li *et al*., *Sustain Mater Technologies.* **29**, e00305 (2021).
31. M. A. Kramer, *AIChE J.* **37**, 233–243 (1991).
32. L. Breiman, *Mach. Learn.* **45**, 5–32 (2001).
33. S. M. Lundberg *et al*., *Nat. Mach. Intell.* **2**, 56–67 (2020).
34. M. Krzywinski *et al*., *Genome Res.* **19**, 1639–1645 (2009).
35. R. Gómez-Bombarelli *et al*., *ACS Cent. Sci.* **4**, 268–276 (2018).
36. G. Qian *et al*., *ACS Energy Lett.* **6**, 687–693 (2021).
37. L. S. Shapley, "A value for n-person games" (RAND Corporation, 1953); https://www.rand.org/pubs/papers/P295.html.
38. S. Lundberg, S.-I. Lee, A unified approach to interpreting model predictions arXiv:1705.07874 [cs.AI] (2017).
39. J. Hu *et al*., *J. Power Sources* **454**, 227966 (2020).
40. J. Billaud, F. Bouville, T. Magrini, C. Villevieille, A. R. Studart, *Nat. Energy* **1**, 16097 (2016).
41. J. S. Sander, R. M. Erb, L. Li, A. Gurijala, Y.-M. Chiang, *Nat. Energy* **1**, 16099 (2016).
42. C. Lei, Z. Xie, K. Wu, Q. Fu, *Adv. Mater.* **33**, e2103495 (2021).
43. J. Li *et al*., Data for: Dynamics of particle network in composite battery cathodes, Zenodo (2022); https://doi.org/10.5281/zenodo.5888945.

ACKNOWLEDGMENTS

Funding: The work at SLAC National Accelerator Laboratory is supported by the Department of Energy, Laboratory

Directed Research and Development program under contract DE-AC02–76SF00515. The work at Purdue University is supported by the National Science Foundation under grant no. DMR-1832707. The work at Virginia Tech is supported by the National Science Foundation under grant no. DMR-1832613. **Author contributions:** Conceptualization: Y.L., K.Z., and F.L.; Investigation: J.L., N.S., Z.J., Y. Y., F. M., Z. X., D.H., D.R., P.P., P.C., F.L., K.Z., and Y.L.; Methodology: J.L., N.S., F.L., K.Z., and Y.L.; Resources: F.L., K.Z., and Y.L.; Writing – original draft: J.L., N.S., K.Z., F.L., and Y.L. All authors reviewed, edited, and approved the manuscript. J.L. and N.S. contributed equally to this work. **Competing interests:** None declared. **Data and materials availability:** The source code supporting the findings of the study is available at (*43*). All (other) data needed to evaluate the conclusions in the paper are present in the paper or the supplementary materials.

SUPPLEMENTARY MATERIALS

science.org/doi/10.1126/science.abm8962
Materials and Methods
Figs. S1 to S12
Table S1
References (*44*–*48*)

19 October 2021; accepted 25 February 2022
10.1126/science.abm8962